



Research paper

Dual couples Bi metal depositing and Ag@AgI islanding on BiOI 3D architectures for synergistic bactericidal mechanism of *E. coli* under visible light



Shangbo Ning, Huaxiang Lin*, Yuecong Tong, Xiaoyan Zhang, Qianying Lin, Yiqiu Zhang, Jinlin Long, Xuxu Wang*

Research Institute of Photocatalysis, State Key Laboratory of Photocatalysis on Energy and Environment, Fuzhou University, Fuzhou 350002, PR China

ARTICLE INFO

Article history:

Received 30 August 2016
Received in revised form 28 October 2016
Accepted 3 November 2016
Available online 4 November 2016

Keyword:

Ag@AgI/Bi-BiOI
Synergism
Photocatalysis
Disinfection
Mechanism

ABSTRACT

Ag@AgI/Bi-BiOI (AABB) three-dimensional (3D) nanoarchitectures, synthesized by solvothermal reaction and photoreduction method, were used as high-effective visible light driven (VLD) photocatalysts for the inactivation of *Escherichia coli* K-12 (*E. coli* K-12) and were characterized by TEM, SEM, XRD, BET, XPS and DRS. The prepared 30%AABB exhibited the best bacteria disinfection efficiency, and the quantity of viable bacteria could almost inactivate after being illuminated for 18 min. The enhanced photocatalytic performance can be attributed to the improved separation efficiency of the photogenerated electron-hole pairs because of its multivariant nanoarchitectures with simultaneous electron transfers ($\text{Bi} \rightarrow \text{BiOI}_{\text{CBM}} \rightarrow \text{Ag} \rightarrow \text{AgI}_{\text{VBM}}$). Furthermore, the SEM technology was applied to certify the photocatalytically lethal effect to *E. coli* K-12 and the rupture of bacterial membranes. In this work, the antibacterial mechanism was studied by employing Photoluminescence (PL), Photoelectrochemical Techniques, Electron Spin Resonance (ESR), and scavengers of different reactive species, revealing the pivotal roles of h^+ , e^- , and $\cdot\text{O}_2^-$ in the photocatalytic process. This study indicated that the fabricated AABB photocatalysts could be potentially utilized to disinfect bacteria in water.

© 2016 Elsevier B.V. All rights reserved.

1. Introduction

At present, wastewater pollution has a great influence on human survival and social development, which involves not only inorganic and organic chemical pollutants but also bacteria and pathogenic microorganisms [1,2]. Microbial pollution has always been hazardous to the human beings. Death, disease and disability are caused by pathogenic microorganisms every day. The ideal alternative method would be to perfect sanitation infrastructure, however, this is often accompanied by large cost and could not be fast accomplished. Short-term solutions for water disinfection, such as chlorination and filtration techniques inevitably append noxious disinfection by products (DBPs), which probably emerge from an unconscious health hazard. Nevertheless, since Matsunaga firstly reported that TiO_2 photocatalyst could disinfect bacterial in water, using inorganic antimicrobial photocatalytic materials for economical, clean, and sustained water purification has become an appropriate approach [3].

Oxidative stress induced by reactive oxygen species (ROS) generation in semiconductor nanoparticles systems is promoted to be the main mechanism of their antibacterial activity [4,5]. Photo-generated electrons in the conduction band (CB) of semiconductor particles are trapped by the O_2 to form reactive $\cdot\text{O}_2^-$. At the same time, the holes left in valance band (VB) of semiconductor particles or react with H_2O to form $\cdot\text{OH}$ radicals. Singlet oxygen ($^1\text{O}_2$) can also be mostly produced indirectly from the aqueous reaction of $\cdot\text{O}_2^-$ [6]. All of these species, which are known as ROS, can irreversibly damage biomolecules and inactivate bacteria [4]. Hence, inorganic semiconductor photocatalysis has attracted growing concern as a promising technique for the inactivation of bacterial contaminations due to the powerful photocatalytic ability.

However, TiO_2 with large band gap can only exhibit high photocatalytic activity under UV light, which only accounts for 5% of the whole solar spectrum. In addition, the fast recombination rate of the photoexcited electrons and holes in TiO_2 leads to its limited quantum efficiency [7,8]. Thus, developing modified TiO_2 [9,10] and novel semiconductors [11] or metallic nanocomposites [12–14] with higher VLD photocatalytic ability has become a crucial issue.

Moreover, novel VLD antimicrobial photocatalysts, such as Ag_3PO_4 [15], BiVO_4 [11] and BiOX ($\text{X} = \text{Br}, \text{I}$) [7,16,17] had been put

* Corresponding authors.

E-mail addresses: lhx@fzu.edu.cn (H. Lin), xwang@fzu.edu.cn (X. Wang).

forward and attracted great attention. Among them, Bismuth oxyhalides, BiOX have been the most popular because of their unique structure of alternate $[\text{Bi}_2\text{O}_2]$ layers sandwiched with the X-slabs and self-built internal static electric fields between positive slabs and anionic slabs. BiOI seems to be more desirable photocatalyst since it has the strongest absorption in the visible light region due to the narrowest band gap (~ 1.8 eV). However, the small band-gap also leads to the high recombination efficiency of photogenerated electrons and holes. Therefore, it is of great significance to find the photocatalysts that can effectively suppress the recombination of photogenerated electron-hole pairs of BiOI, and then improve their VLD photocatalytic activity [18,19]. Zhou's group [20] prepared the typical BiOI 2D plate and 3D flower with exposed (0 0 1) facets that were degraded Methyl Orange (MO) as substrates on the growth of Ag quantum dots. Li and his group [21] reported the obtained Ag/AgI/BiOI showed excellent photocatalytic activity for the decomposition of Methylene Blue (MB) and O-Nitrophenol (OPN) under visible light irradiation. In these systems, the loaded noble metal nanoparticles demonstrated localized surface plasmon resonance (SPR) effect [22,23] as well as electron trapping effect [24,25], which will notably improve the photocatalytic activities of substrates. More importantly, Bismuth (Bi) is a semimetal with a very small band gap, possessing a high anisotropic Fermi surface, low carrier density, small carrier effective mass, and a long carrier mean free path [26,27]. Recently, it was demonstrated that the semimetallic Bi also showed the plasmonics properties similar to those noble metals [28,29]. Compared to noble metal, Bi is cheaper and more available. Moreover, Bi is one significant component of BiOI, which is conducive to in situ reduction and one step synthesis of Bi nanoparticle modified BiOI with better lattice matching in their interface. Meanwhile, the formation of the low oxidation state contributed to produce oxygen vacancy in the crystal lattice [12], which is beneficial to the transfer of charges, and thus enhances the photocatalytic activity of the semiconductor. However, to the best of our knowledge, plasmonic Bi metal and Ag@AgI synergistic effect on VLD photocatalytic bacterial inactivation properties of AABB have never been attempted yet. Additionally, the underlying bacterial inactivation mechanism of AABB photocatalysts (AABBs) under VL irradiation has never been investigated in detail.

It is generally known that bacteria inactivation owes to the oxidation or damage of the organic molecules of their cellular membranes and the nucleic acids of their DNA [30]. In this work, for the first time, we successfully achieved a facile synthesis of plasmonic Bi metal deposits and Ag@AgI islands on high-responsive BiOI 3D architectures through solvent reduction and in situ ion-exchange followed by solvothermal reaction and photoreduction method. The synergistic photodynamic bacterial inactivation activities of these ABBs were assessed using a model bacterium, *E. coli* K-12. The dominating reactive species involved in the synergistic bactericidal activity were also identified. As a result, a reasonable mechanism was proposed to well explain the significant transfer of photogenerated electrons and holes in the VLD-synergistic photocatalytic bacterial inactivation performance between the Bi metal and the Ag@AgI exposed BiOI nanoarchitectures.

2. Experimental

2.1. Materials

Bismuth nitrate pentahydrate ($\text{Bi}(\text{NO}_3)_3 \cdot 5\text{H}_2\text{O}$, AR), potassium iodide (KI, AR), silver nitrate (AgNO_3 , AR), ethylene glycol (AR), Polyvinyl Pyrrolidone (PVP, AR), citric acid (CA, AR) were purchased from Sinopharm Chemical Reagent Co., Ltd., China without any further purification. The bacterial cells were cultured in Mueller-Hinton broth solution at 37°C for 18 h and immediately diluted. The

concentration of cell density is $10^{6.5}$ cfu (colony forming unit)/ml. Deionized water was also used in all the experiments. All glass apparatuses used were washed with deionized water, and then autoclaved at 121°C for 20 min.

2.2. Synthesis of bi-BiOI and Ag@AgI/Bi-BiOI

4 mmol $\text{Bi}(\text{NO}_3)_3 \cdot 5\text{H}_2\text{O}$ was added into an 40 ml ethylene glycol (EG) solution containing 4 mmol KI with 0.5 g PVP and 0.1 g CA. After stirring for 1 h, the mixture solution was transferred into a 100 ml Teflon-lined stainless autoclave. The autoclave was heated at 180°C for 3 h under autogenous pressure, and then it was cooled to room temperature naturally. The resulting products of Bi-BiOI were gathered and rinsed with deionized water and ethyl alcohol thoroughly, and finally dried at 60°C .

The AgI/Bi-BiOI hybrid composite was prepared by an in situ ion-exchange route [22]. Bi-BiOI sample (1 mmol) was dispersed in 40 ml ethylene glycol containing AgNO_3 (0.1 mmol, 0.3 mmol, 0.5 mmol), and vigorously stirred for 12 h. The obtained AgI/Bi-BiOI samples were then reduced by UV irradiation for 10 min to reduce adsorbed Ag^+ to Ag^0 and the generated ABB products were abbreviated as 10%AABB, 30%AABB and 50%AABB. The as-obtained ABB was collected, washed with deionized water and absolute ethanol for several times, and then dried in vacuum drier at 60°C overnight. For comparison, we also prepared Ag@AgI sample through direct precipitation of AgNO_3 and KI aqueous solution followed by UV irradiation reduction for 10 min.

2.3. Characterization

Crystal structure identification was performed using Bruker D8 X-ray diffractometer (XRD) with $\text{Cu K}\alpha$ radiation operating at 40 kV and 40 mA. The morphologies of ABBs were observed by an FEI Nova Nano-SEM 230 field-emission scanning electron microscope (SEM). Microstructures, selected area electron diffraction (SAED) and elemental mapping patterns were investigated using Tecnai G2 F20 S-TWIN (FEI company) Transmission electron microscopy (TEM) with a field emission gun at 200 kV. The Brunauer-Emmett-Teller (BET) specific surface areas of the samples were evaluated on the basis of nitrogen adsorption isotherms using a Micromeritics ASAP 2020 gas adsorption apparatus (USA). Diffuse reflection spectra (DRS) of the samples were recorded on a Varian Cary-500 spectrophotometer, using BaSO_4 as the reference. The PL spectra were obtained using an Edinburgh Analytical Instrument FL-FSTCSPC920 Spectrophotometer. The detection of activated species was conducted by the spin-trapping ESR measurement on a Bruker model A 300 spectrometer. Photoelectrochemical characterization was conducted on a ZENNIUM electrochemical workstation (Zahner, Germany) with a standard three-electrode system. The prepared samples served as the working electrode with an active area of ca. 0.25 cm^2 . The counter and reference electrodes were Pt plate and Ag/AgCl electrode and 0.2 M Na_2SO_4 (pH = 6.8) was used as electrolyte. A 300 W Xenon lamp was used to provide VL light ($\lambda \geq 420\text{ nm}$).

2.4. Photocatalytic disinfection tests

E. coli-12 was used as a model bacterium to investigate the antimicrobial activity of Bi-BiOI and ABBs. The bacterial cells were cultured to a mid-log phase in Mueller-Hinton (MH) broth at 37°C . During each test, 40 ml bacterial PBS solution ($1 \times 10^{6.5}$ cfu/ml) was poured into a pyrex glass reactor which contained the solid photocatalyst at 0.5 mg/mL, and was stirred in the dark for 15 min to keep the adsorption-desorption equilibrium. These suspensions were then irradiated with a Xe lamp equipped with a long-pass cut-off filter VL (300 W, $\lambda \geq 420\text{ nm}$). Aliquots (0.5 ml) of suspension were

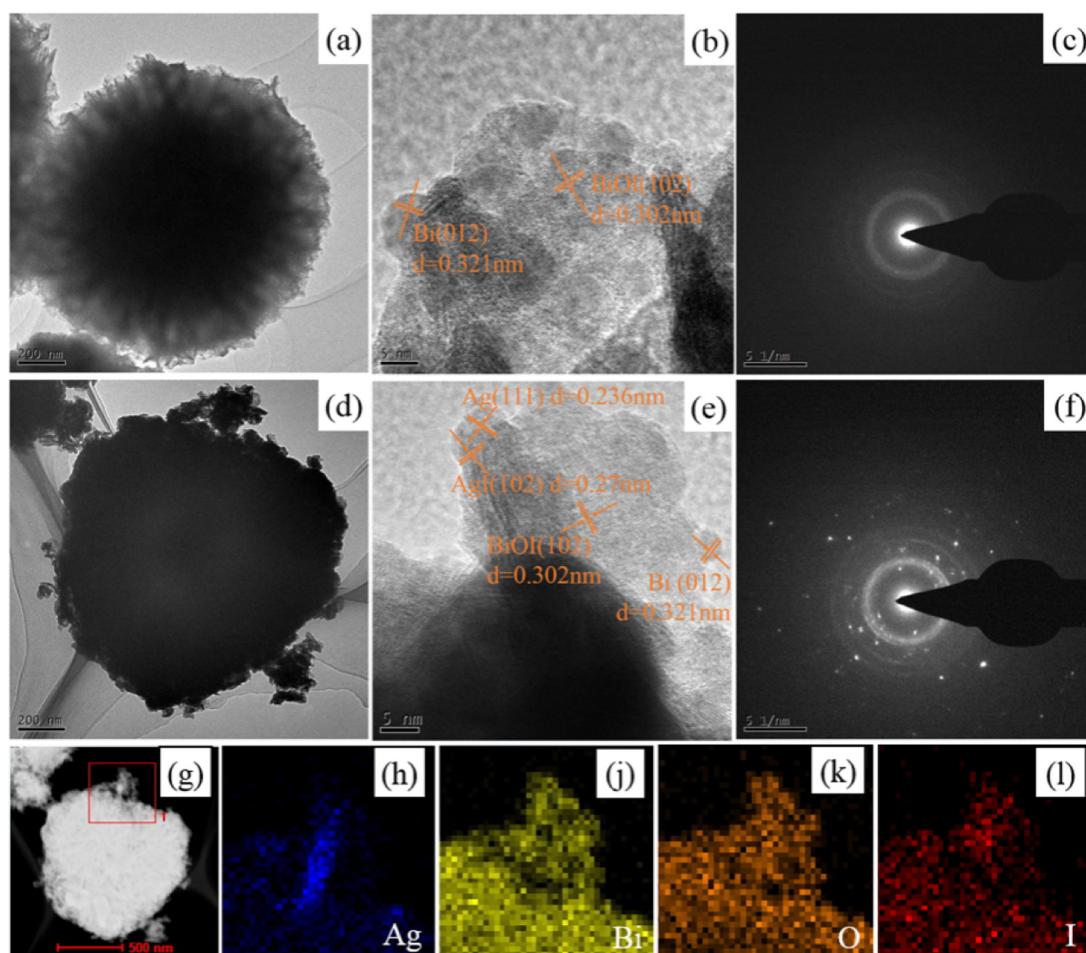


Fig. 1. TEM images of Bi-BiOI (a), 30%AABB (d); HRTEM of Bi-BiOI (b), 30%AABB (e); (c) and (f) are the corresponding SAED pattern; and corresponding energy-dispersive X-ray spectroscopy (EDS) elemental mapping for Ag (h), Bi (j), O (k), and I (l). The scale bar is 500 nm of (g) in (h–l).

withdrawn at regular time intervals, diluted and spread on freshly prepared agar plates and incubated at 37 °C for 36 h.

2.5. SEM observation of bacteria

Bacterial SEM was used to visualize the changes of cell morphologies. The phototreated bacteria at different irradiation time intervals (0, 6, and 18 min) and normal bacteria were fixed with 2.5% glutaraldehyde solution at 4 °C overnight. The samples were dehydrated with 20, 40, 60, 80, and 100% ethanol for 30 min one by one, respectively. Finally, the obtained samples were lyophilized for SEM.

3. Results and discussion

3.1. Properties of bi-BiOI and Ag@AgI/Bi-BiOI

The typical TEM and SEM images of Bi-BiOI and AABBs were shown in Fig. 1 and Fig. 1S. As can be seen from Fig. 1a, the 3D hierarchical Bi-BiOI architecture displayed flake-like shapes with high transparency and some distinct wrinkles at the edge. In Fig. 1b, the lattice fringes of Bi metal and BiOI were 0.321 and 0.302 nm, which in accordance with the interplanar spacing of (0 1 2) plane and (1 0 2) plane of Bi nanoparticles and BiOI architectures, respectively, indicating that Bi-BiOI sample was highly crystalline. Similarly, as shown in Fig. 1d, compared to 1a, Ag@AgI nanoparticles were well dispersed on the hierarchical surface of Bi-BiOI. The lattice fringes of Ag and AgI (in Fig. 1e) were 0.236 and 0.27 nm, which were assigned

to the crystal planes of Ag (1 1 1) and AgI (1 0 2). The corresponding selected area electron diffraction (SAED) (the images of Fig. 3c and f) indicates that the products both are polycrystalline. Fig. 1g was a representative image of 30% AABBB with a corresponding energy-dispersive X-ray spectroscopy (EDS) elemental mapping for Ag (Fig. 1h), Bi (Fig. 1j), O (Fig. 1k), and I (Fig. 1l). In this elemental map, the brighter area indicated a higher concentration of this corresponding element. Obviously, the elements of Bi, O, I, and Ag were well-dispersed in the 30%AABB, further confirming the successful synthesis of AABBB composite photocatalysts. In Fig. 1a, the mean width of the Bi-BiOI was approximately 1 μm. Many nanoparticles anchored on the 3D surface were observed, and these nanoparticles were confirmed to be metallic Bi particles, which corresponds well to the previous TEM discussion. Fig. S1b, c and d presented the SEM images of the hierarchical AABBB microspheres synthesized by the in situ ion-exchange and photoreduction method after being modified with Ag@AgI. As the amount of Ag@AgI in the composites varied from 10% to 50%, the amount of Ag@AgI nanoparticles on the 3D substrates gradually increased, while the initial shape and size of the Bi-BiOI construction were almost maintained.

The X-ray diffraction (XRD) patterns of the photocatalysts were displayed over the range of $15^\circ < 2\theta < 80^\circ$ in Fig. 2a. All the peaks of the BiOI and AgI samples could be readily indexed to the standard tetragonal phase of BiOI (space group P4/nmm (1 2 9), JCPDS Card No. 10–0445) and the cubic phase of AgI (space group Fm–43 m (2 1 6), JCPDS Card No. 09–0399). By introducing Bi and Ag@AgI into the BiOI, an obvious change in XRD pattern was observed. Notably, the intensity of (1 0 2), (1 1 0) peak of BiOI gradually decreased

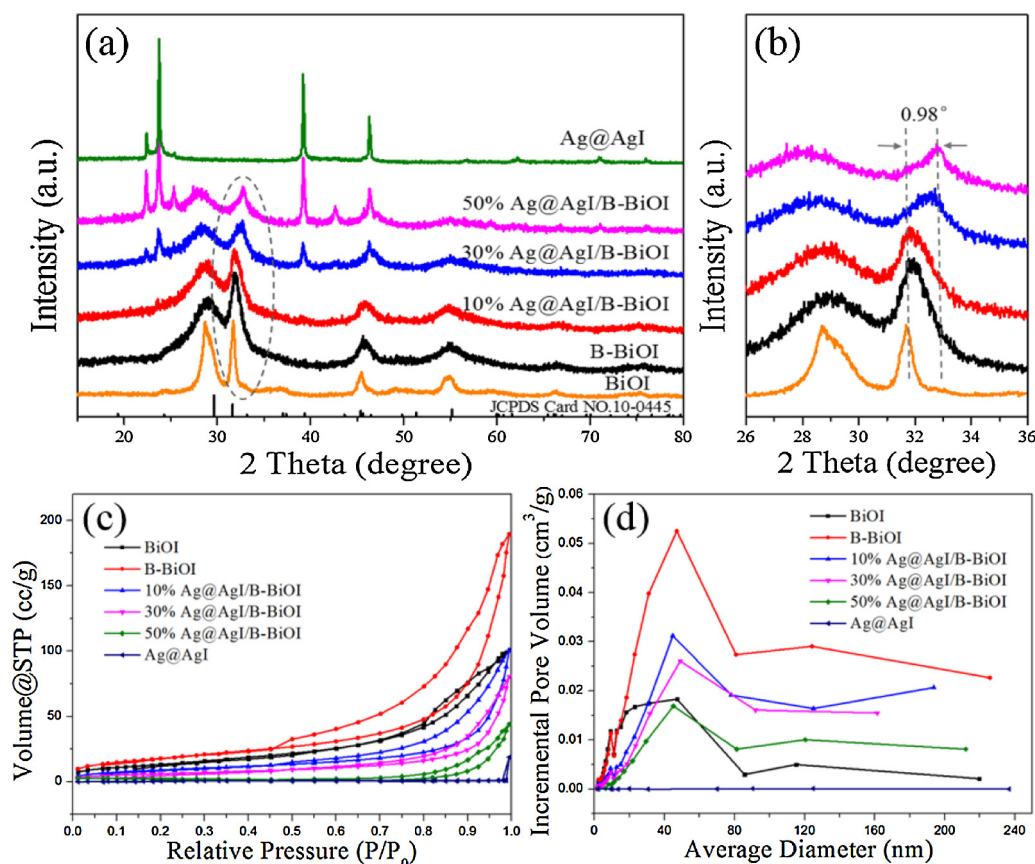


Fig. 2. XRD patterns (a), (b), N₂ adsorption-desorption isotherms (c), and pore size distributions (d) of the photocatalysts.

with an increase of Ag@AgI concentration, which implies that the crystallinity of crystals was damaged. On the contrary, the characteristic peaks of AgI, such as (1 1 1), (2 2 0), (3 1 1) and (3 3 1) peaks, appeared when the amount of Ag@AgI was high, as observed for AABBs. This observation strongly evidenced that elementary AgI was in situ ion-exchange reduced from BiOI. Another absorbing phenomenon surveyed from the XRD patterns is that the (1 1 0) peak of BiOI shows a slight right-shift (0.98°) with increasing the amounts of Ag@AgI (Fig. 2b), which was on the basis of Bragg law ($n\lambda = 2d \sin 2\theta$), the increased 2θ intends an shrunken lattice spacing of one crystal [31], and a certain impurity probably doped into the lattice of BiOI matrix. Moreover, no diffraction peaks of Ag⁰ and Bi⁰ appeared in the patterns probably due to its low content or high dispersity, and no other peaks derived from impurities were observed, suggesting the good crystalline of the as-prepared samples.

In Fig. 2c and d, the N₂ adsorption-desorption isotherms and the pore diameter distribution of prepared samples were shown, respectively. The correlative data of the Brunauer-Emmett-Teller (BET) specific surface areas and pore volumes were displayed in Table S1. It is obvious that Ag@AgI without the hysteresis loop should belong to a typical type II curve, suggesting that it is nonporous microstructure. However, according to the IUPAC classification, the adsorption-desorption isotherms of BiOI, Bi-BiOI, and AABBs with hysteresis loops in 0.7–1.0, 0.45–1.0 and 0.5–1.0, respectively, could be classified as typical type IV. The surface areas of BiOI, Bi-BiOI, 10%AABB and 30%AABB, 50%AABB, and Ag@AgI were 50.3, 66.1, 33.7, 26.8, 18.6, and 2.57 m²/g, respectively (Table S1). Thus, the porous nano-structures were formed in BiOI, Bi-BiOI and AABBs, and surface areas of AABBs nanoarchitectures kept slightly decreasing with the rising doping ratios of Ag@AgI. In the Barrett-Joyner-Halenda (BJH) pore size distributions, all the

samples showed wide distributions (20–90 nm), and the porous diameters of maximum distributions within Bi-BiOI, 10% AABBs, 30% AABBs, and 50% AABBs were in a range from 45.4 to 43.8, 45.7, and 36.7 nm, respectively. Compared with Ag@AgI, it was obvious that the pore diameter was enhanced while coupling Ag@AgI with Bi-BiOI. Therefore, the suitable surface areas and a nanoporous structure of AABBs can serve as better efficient transport paths and provide more adsorption sites for reactants and products in the photocatalytic reaction process [8,32], which is expected to be in agreement with their enhanced disinfection efficiencies.

The chemical states of the BiOI, Bi-BiOI and AABBs were investigated by XPS analysis. As shown in Fig. 3a, only C, Bi, O, I and Ag were detected in the sample. The C 1s peak at around 284.6 eV can be attributed to the signal from carbon contained in the instrument and was used for calibration [33]. Fig. 3b showed that both Ag 3d_{5/2} and 3d_{3/2} peaks could be divided into two individual peaks. Among them, the peaks at 367.6 eV and 373.5 eV were attributed to Ag⁺ in AgI [34], and those at 368.6 eV and 374.5 eV were assigned to Ag⁰ species [35]. The Bi 4f XPS spectra of BiOI, Bi-BiOI and 30%AABB were shown in Fig. 3c, revealing Bi 4f_{5/2} and Bi 4f_{7/2} characteristic peaks at 164.7 eV and 159.1 eV, respectively. In comparison with BiOI, a slight binding energy left-shift of Bi 4f peaks occurred over Bi-BiOI and 30%AABB, suggesting that the coordination environment of Bi³⁺ ions may be changed [31]. Moreover, an additional doublet with binding energy of 162.5 eV and 157.2 eV for Bi 4f (inset of Fig. 3c) was also observed, suggesting that certain parts of bismuth existed in the metallic Bi valence state [27]. It indicated that the Bi³⁺ was partially reduced to the lower valence state by the solvothermal composites synthesized method. Therefore, after being partially reduced from the 3D-BiOI, the samples of Bi-BiOI and AABBs contained not only BiOI but also metallic Bi. The XPS spectrum of the I 3d region of 30%AABB (Fig. 3d) revealed doublet

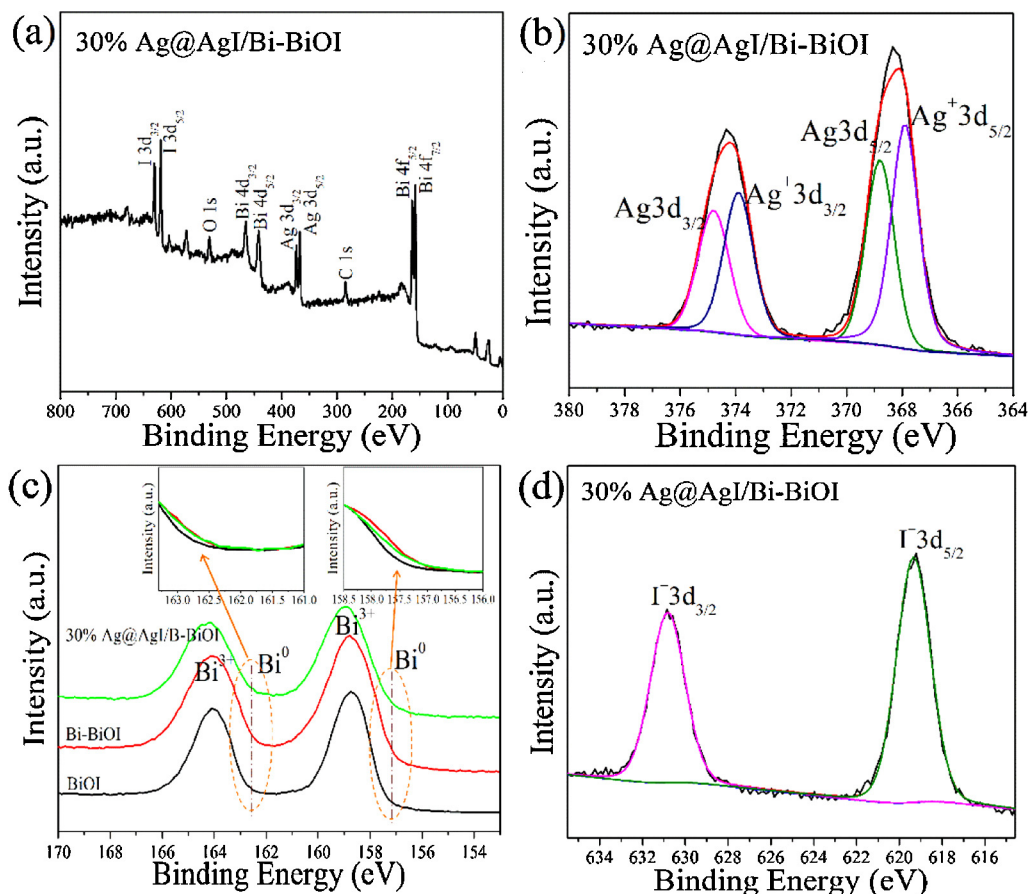


Fig. 3. High-resolution XPS spectra: (a) overall XPS spectra of 30%AABB, (b) Ag 3d of 30%AABB, (c) Bi 4f of BiOI, Bi-BiOI and 30%AABB, and (d) I 3d of 30%AABB.

peaks at 630.2 eV ($I 3d_{5/2}$) and 618.6 eV ($I 3d_{3/2}$), which are assigned to I^- in AgI [34]. The result of XPS analysis revealed the coexistence of Bi-BiOI and Ag@AgI in the AABB composite materials.

The optical absorption properties of the prepared samples investigated by UV–vis spectrophotometer were shown in Fig. 4. With a small amount of plasmonic Bi metal deposition on the product, its color shallowed from red to orange, which implies that the intrinsic optical properties have changed (inset of Fig. 4a). We observed that the pure BiOI showed an absorption edge around 688 nm and the Bi-BiOI sample showed an absorption edge around 626 nm (in Fig. 4a). Compared with the spectra of pristine Ag@AgI, the spectra of the AABBs showed a strong broad absorption band between 450 nm and 600 nm that covered almost entire visible range, which in turn guaranteed their high visible photocatalytic disinfection ability (in Fig. 4b). The dramatic visible light absorption enhancement with a convex peak around 550 nm was attributed to the surface plasmon resonance (SPR) of metallic Ag^0 nanoparticles, which result from the partial reduction of AgI upon light exposure [36].

3.2. Photocatalytic disinfection performance

The photocatalytic disinfection activity of prepared samples was evaluated by the inactivation of *E. coli* for different time intervals (before 15, 0, 12, 18, 24, 36, 48, and 60 min) in aqueous buffer solution under VL. As can be seen in Fig. 5a, under dark conditions, all of the photocatalysts showed negligible disinfection efficiencies during the experimental duration, indicating that AABBs did not contain bactericidal capacity without light irradiation. Similarly, there were almost no *E. coli* that was inactivated in the light control (in Fig. S2). Fig. 5b showed the disinfection activity of BiOI,

Bi-BiOI and AABBs for *E. coli* under visible light. It can be seen that BiOI alone did slightly cause cell density decrease, indicating that without the presence of Bi and Ag@AgI, BiOI did not contain antibacterial property within 60 min. Over a period of 18 min of visible light irradiation, both Bi-BiOI and Ag@AgI displayed very low disinfection efficiencies, and the cell density of viable bacteria was approximately $10^{6.10}$ and $10^{6.15}$, respectively. Nevertheless, for 10% AABB, 30% AABB and 50% AABB, the quantity of viable bacteria was $10^{4.90}$, $10^{0.15}$ and $10^{3.20}$ after photocatalytic disinfection, respectively (in Fig. 3b). Obviously, the disinfection efficiencies for AABBs had improved significantly compared with those of Bi-BiOI or Ag@AgI. Among all of the materials, 30% AABB always exhibited the best response at each time interval, and almost all of the bacteria could be killed after 18 min light irradiation, which could guarantee its best ability of disinfection.

According to the previous research, two main mechanisms are the most probable cause of the photocatalytic inactivation of bacteria. The first proposed by Matsunaga' group holds oxidation of the intracellular CoA, because of direct contact between the target cells and the photocatalysts, which inhibits the cell respiration and then causes cell death [3]. The second assumed killing mechanism suggests that bacterial inactivation is caused by a disorder in the cell permeability and the decomposition of the cell walls [37]. To further understand the destruction process of normal bacterial cells in the AABB photocatalytic system under VLD, the morphology and microstructure of *E. coli* at different time intervals were examined by SEM study. Fig. 6a showed a typical SEM image of *E. coli* before inactivation treatment that had an equably colored interior and a well-preserved cell wall. However, after the damage of *E. coli* by the 30%AABB under illumination for 6–18 min (Fig. 6b–d),

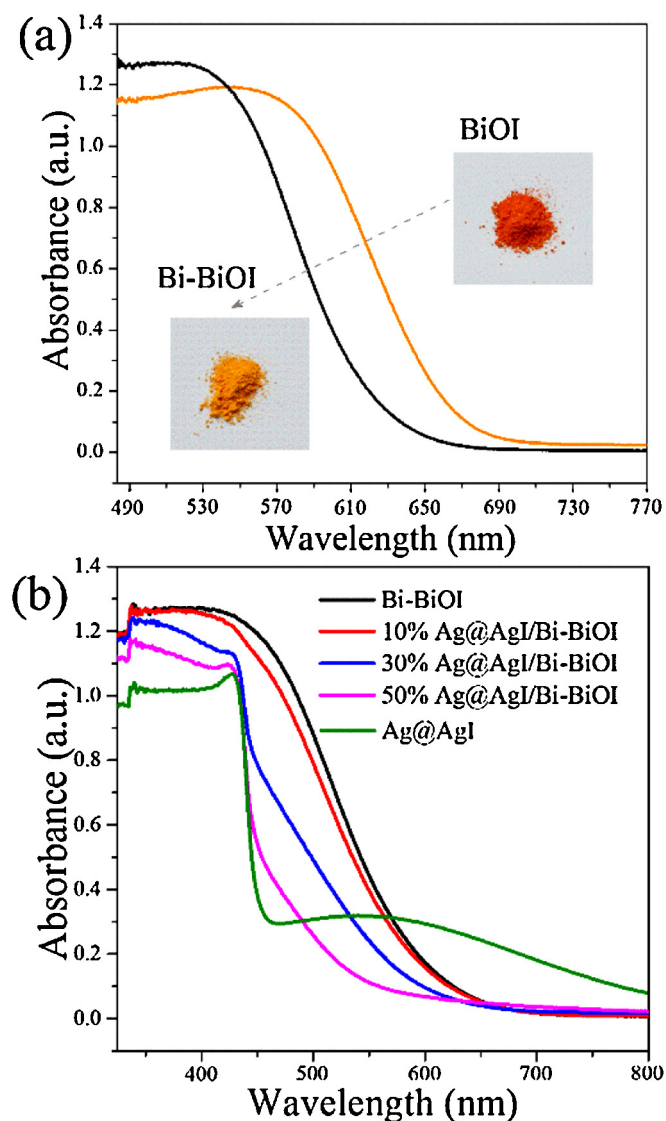


Fig. 4. UV-vis DRS of (a) BiOI and Bi-BiOI (Inset: photos of the corresponding samples showing the color change from BiOI to Bi-BiOI after the deposition of metallic Bi), (b) Bi-BiOI, Ag@AgI and AABBB architectures.

the morphology of *E. coli* cell was progressively fragmented. After 6 min irradiation (Fig. 6c), the cell is still intact but part of the cell wall structure slightly appears depression, indicating initial damage to the cell wall and cytoplasmic membrane by active species [11]. Obviously, after 18 min irradiation, Fig. 6d shows that the cell membrane of Rod-shaped *E. coli* became deformed and wrinkled with some small pits [8], indicating that the intracellular content had leaked out and active species such as e^- , $\cdot O_2^-$, $\cdot OH$, H_2O_2 and h^+ , which played important roles in photocatalytic reaction had been rapidly produced.

3.3. The mechanism of synergistic photocatalytic disinfection

PL, photoelectrochemistry, and active species trapping experiments were conducted to survey the charge transfer behavior as well as the photocatalytic disinfection mechanism.

The room temperature PL spectra surveyed at the strongest excitation wavelength 350 nm showed that the modified AABBB samples had a lower recombination rate of electron-hole pairs than pure BiOI and Bi-BiOI, as they generated a weaker PL peak intensity emitted at 530 nm (Fig. 7a). Generally, low recombination rate of

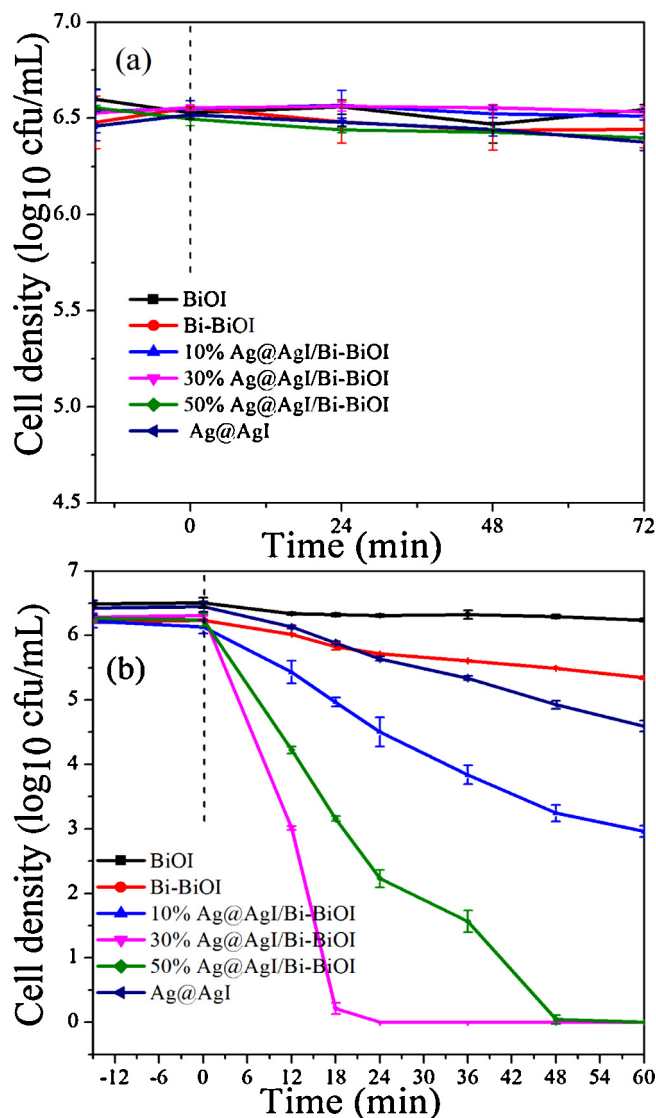


Fig. 5. *E. coli*-12 ($10^{6.5}$ cfu/mL) inactivation by prepared photocatalysts; (a) in the dark and (b) under visible light (≥ 420 nm); Error bars represent standard deviations from triplicate experiments ($n=3$).

electron-hole pairs leads to the low fluorescence intensity and high photocatalytic activity [8,12,31]. The 30%AABBB exhibited the lowest peak intensity, indicating that the constructing ratio of 30%Ag@AgI the most effectively suppressed electrons and holes recombination rate among all of ratios, which corresponded to the greatest photocatalytic bactericidal ability.

Photocurrent generation, which has a close relationship with photocatalytic activity, is another valid way to elucidate the charge separation and transfer dynamics of photoelectrons. The generation of photoinduced electrons and holes as well as their high separation and migration efficiency is supposed to be the key process for photocatalytic sterilization [8]. The rapid increase photocurrent response from a light-off to light-on state was mainly due to the fast separation and transfer of the photogenerated electrons on the surface of the working electrode. Fig. 7b showed the photocurrent response of pure BiOI, Bi-BiOI, Ag@AgI and 30%AABBB with illumination of VL. Obviously, the photocurrent density generated by Bi-BiOI was much higher than that by BiOI. As Bi metal nanoparticles were generated from a BiOI 3D-matrix using an in situ solvothermal reduction and the lattice matching in interface were also better as well as a great number of oxygen vacancies

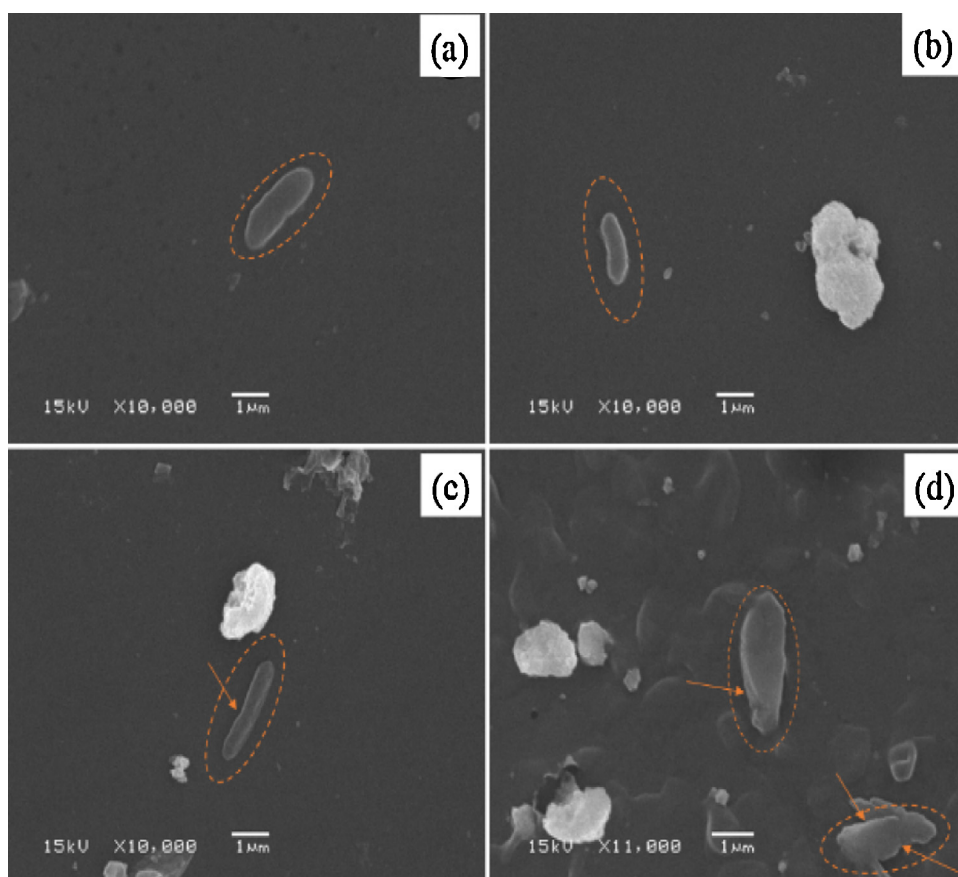


Fig. 6. SEM images of *E. coli* ($10^{6.5}$ cfu/mL) photocatalytically treated with 30%AABB under visible light irradiation for (a) normal cell, (b) 0, (c) 6 and (d) 18 min. The orange circles indicate the deformation, pore-forming, and fracture of *E. coli*. (For interpretation of the references to colour in this figure legend, the reader is referred to the web version of this article.)

could be generated. The presence of oxygen vacancies was confirmed by ESR spectroscopy. The ESR spectrum Bi-BiOI (Fig. 7c) showed a remarkable signal at $g = 2.001$, typical character of oxygen vacancy [38], while no signal was emerged from pure BiOI sample. Better lattice matching and oxygen vacancies are beneficial to the charges transfer, which enhances the photocatalytic activity of the polybasic semiconductor. The 30%AABB exhibited the highest photocurrent response in contrast to the other materials, which possessed the slowest e^- and h^+ recombination rate, matching its best performing activity for photocatalytic bacterial inactivation.

Fig. 7d displayed another important photoelectrochemical property, electrochemical impedance spectroscopy (EIS). The EIS method could determine the separation efficiency of the photo-generated electron–hole pairs, therefore, it can be used to study the ability charge transfer and interface reaction of the excited electrons [8,39]. A smaller arc radius represented a higher charge transfer efficiency on the working electrode surface. In contrast to BiOI, Bi-BiOI and Ag@AgI, 30%AABB showed an even smaller arc radius in the EIS Nyquist plot when the light was on. It indicated that the emigration and transfer of charge carriers had been extensively promoted in the fabricated hybrid 30% AABBB. This inference was in accordance with the PL and photocurrent results.

The disinfection system of *E. coli* involved the generation of the reactive radicals such as $\bullet OH$, $\bullet O_2^-$, H_2O_2 , e^- and h^+ , has been previously reported to attack the bacterial outer membranes and then lead to the inactivation of bacteria [40,41]. Hence, the trapping experiments were carried out during the photocatalytic sterilization reaction for detecting important active species in the presence of 30%AABB with TEMPOL as $\bullet O_2^-$ scavengers, Isopropanol as $\bullet OH$ scavengers, Fe (II)-EDTA as H_2O_2 scavengers, sodium oxalate as h^+

scavengers and Cr(IV) as e^- scavengers, respectively. Before conducting the experiment, the applied concentration of each one of scavengers was optimized to ensure their best scavenging effect as well as could not cause any inactivation to the normal cell [42]. When isopropanol was added into the disinfection system, the disinfection efficiency had the least change compared with the bacterial inactivation without scavenger, indicating that $\bullet OH$ was not the main reactive species in this inactivation process (Fig. 8). After only addition of Fe(II)-EDTA removing H_2O_2 , some inhibitions to the inactivation efficiency was slightly higher than those of adding isopropanol. Obviously, the addition of sodium oxalate and Cr(VI) significantly inhibited the inactivation of *E. coli* by 30%AABB, which confirmed the significant roles of h^+ and e^- in the inactivation processes where photoinduced electrons and holes could directly attack the *E. coli*. Meanwhile, a relative high concentration electrons on the surface of 30%AABB was formed, which could possibly be transformed into other reactive species in the water, such as $\bullet O_2^-$, $\bullet HO_2$ and H_2O_2 , to further oxidize cell membrane and result in ultimate cell death [43]. Thus, all these active species produced were responsible for the VLD bacterial inactivation.

To further identify the reactive oxygen radicals produced from Bi-BiOI, Ag@AgI and 30%AABB under visible light irradiation, the ESR technique with DMPO as a spin-trapping reagent was applied to obtain information on the active radicals and further confirmed the bacterial inactivation mechanism. As shown in Fig. 9a, no obvious signals could be detected in the dark and under visible light, demonstrating that $\bullet OH$ was actually not a dominating reactive species in the inactivation process. However, Fig. 9b showed that the characteristic peaks (1: 1: 1: 1) of $\bullet O_2^-$ were detected in the methanol dispersion of the as-prepared material, and the inten-

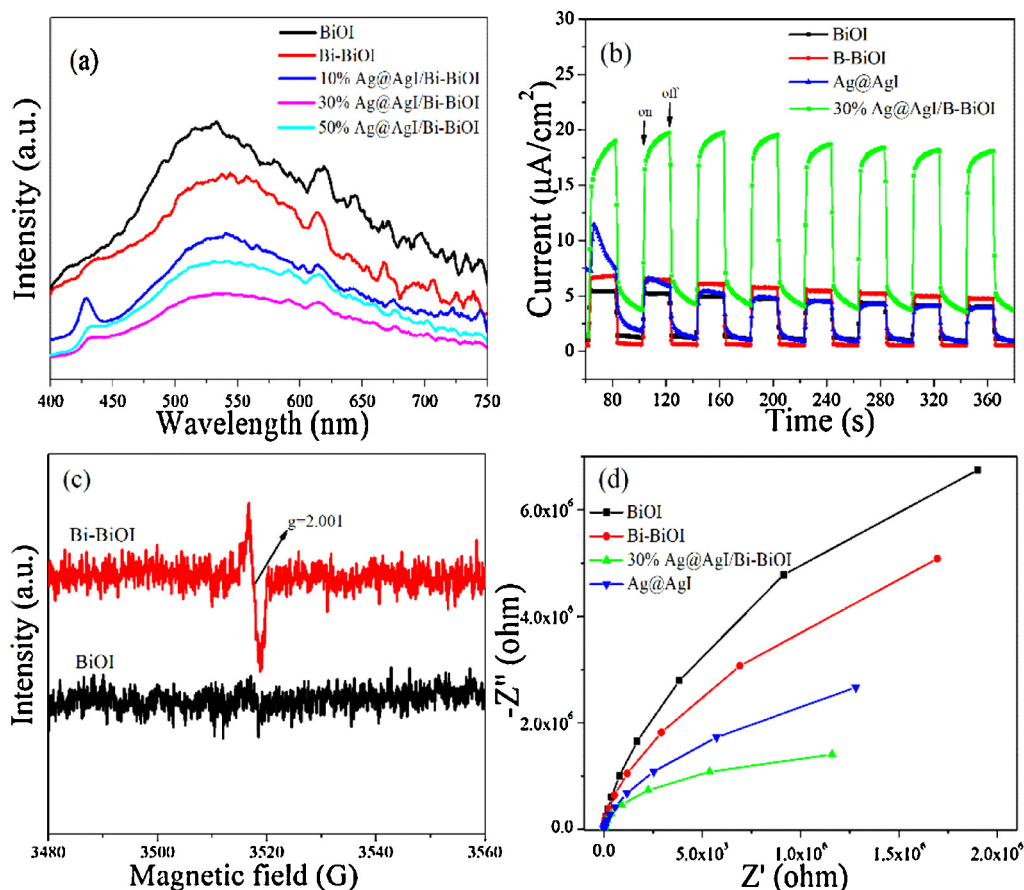


Fig. 7. Photoluminescence spectra of BiOI, Bi-BiOI and AABBs (a), EPR spectra of BiOI and Bi-BiOI (c), Transient photocurrent (b) and (d) EIS Nyquist plots of BiOI, Bi-BiOI, 30% AAB, Ag@AgI electrodes under visible light irradiation.

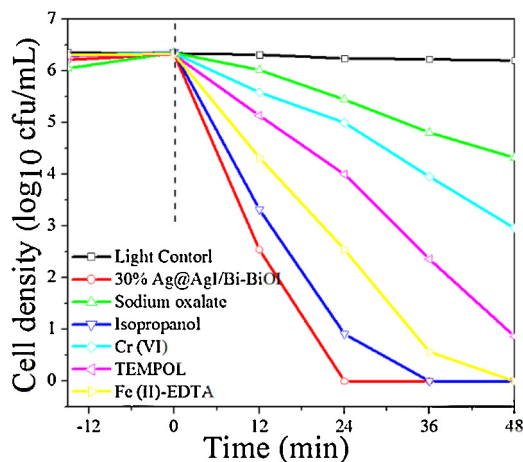


Fig. 8. Photocatalytic inactivation efficiency against *E. coli*-12 (10^{6.5} cfu/mL) with different scavengers (0.5 mM sodium oxalate, 0.5 mM isopropanol, 0.05 mM Cr(VI), 2 mM TEMPOL and 0.1 mM Fe(II)-EDTA) in the presence of 30%AABB (0.5 mg/mL) under visible light irradiation.

sity of 30%AABB was the strongest under visible light irradiation, whereas no $\cdot\text{O}_2^-$ signal was detected in the dark under otherwise identical conditions. These observations clearly provide proof that photogenerated electrons could be retained long enough and react with adsorbed oxygen to produce $\cdot\text{O}_2^-$ and other reactive oxygen radicals, which play important roles in the photocatalytic process.

Then, to understand the mechanism of synergistic photocatalytic bacterial inactivation, it is also important to locate the

positions of the VB maximum (VBM) and the CB minimum (CBM) of the AAB 3D architectures. It has been reported that the significance to locate the positions of the CBM and the VBM for BiOI were +0.6 eV and +2.39 eV [44], while those for AgI were +2.38 eV and -0.42 eV [45], respectively. According to equation: $h\nu = A(h\nu - E_g)^{n/2}$ [12,24], the E_g of Bi-BiOI ($\lambda = 626$ nm) and AgI ($\lambda = 443$ nm) was determined from the formula $g = 1239.8/E_g$ and obtained to be 1.98 eV and 2.8 eV (Fig. S3). The band edges of the Bi-BiOI, AgI and 30%Ag@AgI/Bi-BiOI were measured by VB XPS spectra, as shown in Fig. S4. The Bi-BiOI and AgI presented VBM energy potential at about 1.84 eV and 2.38 eV. The CBM energy potential (E_{CB}) could be determined by $E_{CB} = E_{VB} - E_g$, where E_g is the band gap energy. Thus the E_{CB} of Bi-BiOI and AgI was calculated to be about -0.14 eV and -0.43 eV, respectively. The E_{CB} values of Bi-BiOI was more negative than that of AgI, and the E_{VB} of AgI was more positive than that of Bi-BiOI. The changed E_{VB} of the Bi-BiOI contributed to the matching E_{VB} of the AgI. The unchanged VBM energy band therefore indicated that the E_{CB} of AgI was lowered by 0.01 eV, which was similar to previous research with respect to Li et al. [45] However, the standard redox potentials for $\cdot\text{OH}/\text{H}_2\text{O}$ was reported to be located at +2.73 eV [41]. As a result of their more negative E_{VB} (1.84 eV and 2.38 eV), the photoexcited h^+ in the VB of AAB cannot oxidize H_2O to form $\cdot\text{OH}$, which correlates with the negligible role of $\cdot\text{OH}$ as observed in the scavenger and ESR study.

Considering the above analysis, the electronic potentials of CBM and VBM for Ag@AgI/Bi-BiOI 3D architectures can be determined as shown in Fig. 10. Under illumination of visible light, both BiOI and AgI are simultaneously excited, and the photogenerated h^+ and e^- are activated and separated in their VBM and CBM, respectively. On one hand, because of the SPR effect similar to the noble metal,

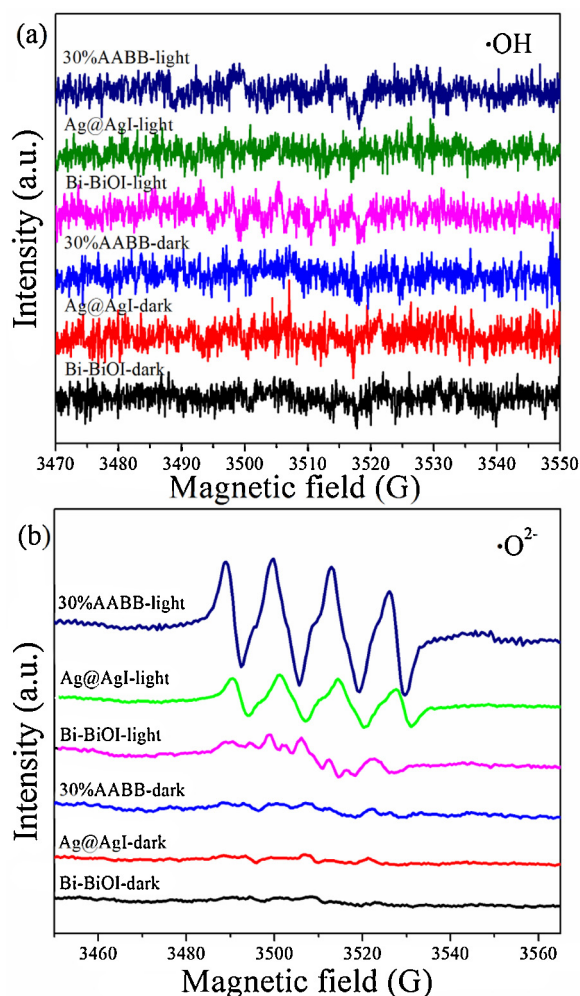


Fig. 9. DMPO spin-trapping ESR spectra recorded with BiOI, Bi-BiOI and 30%AABB photocatalysts in (a) aqueous dispersion for DMPO – $\bullet\text{OH}$ and (b) methanol dispersion for DMPO – $\bullet\text{O}_2^-$, under visible light irradiation.

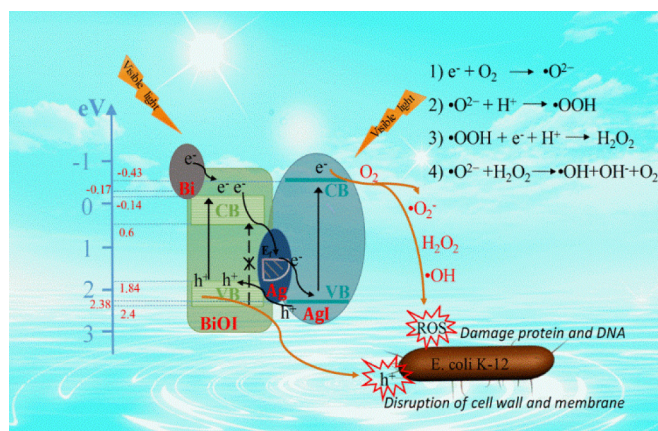


Fig. 10. Band positions and proposed photocatalytic mechanism of ABB 3D architectures.

the metallic Bi contributes the photocatalyst system to absorb more light and generate more active photo-excitons. The SPR effect could accelerate the separation and transport of charge carriers, thus tremendously promoting the photocatalytic activity [31]. As the Fermi level (E_f) of metallic Bi (-0.17 eV) is much more negative than the CBM of BiOI, the electrons can migrate from metal Bi to the

CBM of BiOI (electron transfer I: $\text{Bi} \rightarrow \text{BiOI}_{\text{CBM}}$) due to the potential difference. On the other hand, as the CB potential of BiOI is more negative than that E_f of metallic Ag ($+2.30$ eV), CBM electrons of BiOI (-0.14 eV) easily flow into metal Ag (electron transfer II: $\text{BiOI}_{\text{CBM}} \rightarrow \text{Ag}$) through the formed Schottky barrier. Similarly, VBM holes of AgI also easily flow into BiOI through metal Ag (electron transfer III: $\text{Ag} \rightarrow \text{AgI}_{\text{VBM}}$), as the E_f of Ag is more positive than the V_{BM} of AgI and is negatively to BiOI, which transfers more efficiently than the photogenerated electron-hole recombination between the VBM and CBM of AgI [46,47]. Thus the process of simultaneous electron transfers ($\text{Bi} \rightarrow \text{BiOI}_{\text{CBM}} \rightarrow \text{Ag} \rightarrow \text{AgI}_{\text{VBM}}$) effectively enhance separation holes of BiOI_{VBM} and electrons of AgI_{CBM} , which lead to an enhanced photocatalytic disinfection. The photoinduced electrons would be trapped by O_2 to yield $\bullet\text{O}_2^-$. Then, other oxidizing reactive species, such as H_2O_2 , $\bullet\text{HO}_2$, are generated through the formation of $\bullet\text{O}_2^-$ (Fig. 10). Meanwhile, photo-generated h^+ can still importantly contribute to the bacterial inactivation through direct oxidation. Therefore, these photoinduced reactive species in the system could attack the bacterial cells, oxidize and disrupt of cell membrane, damage protein and DNA, finally lead to the inactivation of the bacteria.

4. Conclusions

Dual couples Bi metal depositing and Ag@AgI islanding on BiOI nanoarchitectures, were successfully synthesized by a facile solvothermal reduction reaction and in situ ion-exchange with photoreduction method. Significantly, the obtained AABB 3D architectures showed considerable efficiency in photocatalytically inactivating *E. coli* K-12 under VL irradiation. A possible sterilization mechanism was proposed for the first time, which depends on simultaneous electron transfers ($\text{Bi} \rightarrow \text{BiOI}_{\text{CBM}} \rightarrow \text{Ag} \rightarrow \text{AgI}_{\text{VBM}}$) among AABB 3D architectures. From this, reactive species, including h^+ , e^- and $\bullet\text{O}_2^-$, played important roles in the photocatalytic disinfection process. On the basis of AABB efficient photocatalytic disinfection activity, the AABB VLD photocatalysts could be widely used for practical application in environmental purification of microbial solution.

Acknowledgements

This work was financially supported by the NSFC (Grant No. 21373051, and U1305242), The Project of Education Office of Fujian province (JK15002), the Science and Technology project of the Education Office of Fujian Province of P.R. China (JA12017), and the National Basic Research Program of China (973 Program, No. 2012CB722607).

Notes and references

Appendix A. Supplementary data

Supplementary data associated with this article can be found, in the online version, at <http://dx.doi.org/10.1016/j.apcatb.2016.11.006>.

References

- [1] M.A. Shannon, P.W. Bohn, M. Elimelech, J.G. Georgiadis, B.J. Marinas, A.M. Mayes, *Nature* 452 (2008) 301–310.
- [2] L.S. Zhang, K.H. Wong, D.Q. Zhang, C. Hu, J.C. Yu, C.Y. Chan, P.K. Wong, *Environ. Sci. Technol.* 43 (2009) 7883–7888.
- [3] T. Matsunaga, R. Tomoda, T. Nakajima, H. Wake, *Fems Microbiol. Lett.* 29 (1985) 211–214.
- [4] Y. Li, W. Zhang, J. Niu, Y. Chen, *ACS Nano* 6 (2012) 5164–5173.
- [5] T. Xia, M. Kovochich, M. Liong, L. Madler, B. Gilbert, H. Shi, J.I. Yeh, J.I. Zink, A.E. Nel, *ACS Nano* 2 (2008) 2121–2134.
- [6] E.J. Corey, M.M. Mehrotra, A.U. Khan, *Biochem. Biophys. Res. Commun.* 145 (1987) 842–846.

- [7] T.S. Jamil, E.S. Mansor, M. Azab El-Liethy, *J. Environ. Chem. Eng.* 3 (2015) 2463–2471.
- [8] Y. Jia, S. Zhan, S. Ma, Q. Zhou, *ACS Appl. Mater. Interfaces* 8 (2016) 6841–6851.
- [9] W. Deng, S. Ning, Q. Lin, H. Zhang, T. Zhou, H. Lin, J. Long, Q. Lin, X. Wang, *Colloid Surf. B Biointer.* 144 (2016) 196–202.
- [10] M. Xing, W. Fang, M. Nasir, Y. Ma, J. Zhang, M. Anpo, *J. Catal.* 297 (2013) 236–243.
- [11] W. Wang, Y. Yu, T. An, G. Li, H.Y. Yip, J.C. Yu, P.K. Wong, *Environ. Sci. Technol.* 46 (2012) 4599–4606.
- [12] S.B. Ning, L.Y. Ding, Z.G. Lin, Q.Y. Lin, H.L. Zhang, H.X. Lin, J.L. Long, X.X. Wang, *Appl. Catal. B-Environ.* 185 (2016) 203–212.
- [13] L. Mohapatra, K. Parida, M. Satpathy, *J. Phys. Chem. C* 116 (2012) 13063–13070.
- [14] W. Wang, J.C. Yu, D. Xia, P.K. Wong, Y. Li, *Environ. Sci. Technol.* 47 (2013) 8724–8732.
- [15] S. Thiyagarajan, S. Singh, D. Bahadur, *Mater. Chem. Phys.* 173 (2016) 385–394.
- [16] X. Hong, M. Li, S. Shan, K.S. Hui, M. Mo, X. Yuan, *Environ. Sci. Pollut. Res. Int.* (2016) 1–9.
- [17] D. Wu, B. Wang, W. Wang, T. An, G. Li, T.W. Ng, H.Y. Yip, C. Xiong, H.K. Lee, P.K. Wong, *J. Mater. Chem. A* 3 (2015) 15148–15155.
- [18] P.D. Cozzoli, R. Comparelli, E. Fanizza, M.L. Curri, A. Agostiano, D. Laub, *J. Am. Chem. Soc.* 126 (2004) 3868–3879.
- [19] K. Sornsanit, M. Horprathum, C. Chananonwathorn, P. Eiamchai, S. Limwichean, K. Aiempnanakit, J. Kaewkhao, *Adv. Mater. Res. Switz.* 770 (2013) 221–224.
- [20] C.C. Zhou, J. Cao, H.L. Lin, B.Y. Xu, B.B. Huang, S.F. Chen, *Surf. Coat. Technol.* 272 (2015) 213–220.
- [21] T.T. Li, S.L. Luo, L.X. Yang, *Mater. Lett.* 109 (2013) 247–252.
- [22] H.F. Cheng, B.B. Huang, P. Wang, Z.Y. Wang, Z.Z. Lou, J.P. Wang, X.Y. Qin, X.Y. Zhang, Y. Dai, *Chem. Commun.* 47 (2011) 7054–7056.
- [23] X.M. Zhou, G. Liu, J.G. Yu, W.H. Fan, *J. Mater. Chem.* 22 (2012) 21337–21354.
- [24] J. Cao, Y.J. Zhao, H.L. Lin, B.Y. Xu, S.F. Chen, *J. Solid. State Chem.* 206 (2013) 38–44.
- [25] W. Xiong, Q.D. Zhao, X.Y. Li, D.K. Zhang, *Catal. Commun.* 16 (2011) 229–233.
- [26] M.C. Gao, D.F. Zhang, X.P. Pu, K.Y. Ding, H. Li, T.T. Zhang, H.Y. Ma, *Sep. Purif. Technol.* 149 (2015) 288–294.
- [27] J.J. Hu, G.Q. Xu, J.W. Wang, J. Lv, X.Y. Zhang, Z.X. Zheng, T. Xie, Y.C. Wu, *New J. Chem.* 38 (2014) 4913–4921.
- [28] J.M. McMahon, G.C. Schatz, S.K. Gray, *Phys. Chem. Chem. Phys.* 17 (2015) 19670–19671.
- [29] H. Chen, S. Chen, X. Quan, Y. Zhang, *Environ. Tci. Technol.* 44 (2010) 451–455.
- [30] A.Y. Booshehri, S. Chun-Kiat Goh, J. Hong, R. Jiang, R. Xu, *J. Mater. Chem. A* 2 (2014) 6209.
- [31] S.X. Yu, H.W. Huang, F. Dong, M. Li, N. Tian, T.R. Zhang, Y.H. Zhane, *ACS Appl. Mater. Interfaces* 7 (2015) 27925–27933.
- [32] H.X. Lin, W.H. Deng, T.H. Zhou, S.B. Ning, J.L. Long, X.X. Wang, *Appl. Catal. B Environ.* 176 (2015) 36–43.
- [33] Z. He, Y. Shi, C. Gao, L. Wen, J. Chen, S. Song, *J. Phys. Chem. C* 118 (2014) 389–398.
- [34] J.Z. Zhang, X. Liu, S.M. Gao, B.B. Huang, Y. Dai, Y.B. Xu, L.R. Grabstanowicz, T. Xu, *Ceram. Int.* 39 (2013) 1011–1019.
- [35] J.G. Yu, G.P. Dai, B.B. Huang, *J. Phys. Chem. C* 113 (2009) 16394–16401.
- [36] H.F. Cheng, W.J. Wang, B.B. Huang, Z.Y. Wang, J. Zhan, X.Y. Qin, X.Y. Zhang, Y. Dai, *J. Mater. Chem. A* 1 (2013) 7131–7136.
- [37] Y. Wang, L. Lin, F. Li, L. Chen, D.H. Chen, C.Y. Yang, M.H. Huang, *Photoch. Photobio. Sci.* 15 (2016) 666–672.
- [38] M.C. Gao, D.F. Zhang, X.P. Pu, H. Li, D.D. Lv, B.B. Zhang, X. Shao, *Sep. Purif. Technol.* 154 (2015) 211–216.
- [39] X. Bai, L. Wang, Y. Wang, W. Yao, Y. Zhu, *Appl. Catal. B Environ.* 152–153 (2014) 262–270.
- [40] L.S. Zhang, K.H. Wong, H.Y. Yip, C. Hu, J.C. Yu, C.Y. Chan, P.K. Wong, *Environ. Sci. Technol.* 44 (2010) 1392–1398.
- [41] D. Wu, W. Wang, T.W. Ng, G.C. Huang, D.H. Xia, H.Y. Yip, H.K. Lee, G.Y. Li, T.C. An, P.K. Wong, *J. Mater. Chem. A* 4 (2016) 1052–1059.
- [42] W.J. Wang, L.Z. Zhang, T.C. An, G.Y. Li, H.Y. Yip, P.K. Wong, *Appl. Catal. B Environ.* 108 (2011) 108–116.
- [43] H.X. Shi, G.Y. Li, H.W. Sun, T.C. An, H.J. Zhao, P.K. Wong, *Appl. Catal. B Environ.* 158 (2014) 301–307.
- [44] B. Chai, Q. Xu, J. Li, K. Dai, *Sci. Adv. Mater.* 6 (2014) 1806–1813.
- [45] J. Yan, C. Wang, H. Xu, Y.G. Xu, X.J. She, J.J. Chen, Y.H. Song, H.M. Li, Q. Zhang, *Appl. Surf. Sci.* 287 (2013) 178–186.
- [46] H. Tada, T. Mitsui, T. Kiyonaga, T. Akita, K. Tanaka, *Nat. Mater.* 5 (2006) 782–786.
- [47] L. Ye, J. Liu, C. Gong, L. Tian, T. Peng, L. Zan, *ACS Catal.* 2 (2012) 1677–1683.